PROCEEDINGS OF SCIENCE

Astrophysical models to interpret the Pierre Auger Observatory data

Juan Manuel González [a,*] **for the Pierre Auger Collaboration**[b]

[a] *Instituto Balseiro, Centro Atómico Bariloche, Comisión Nacional de Energía Atómica*
Consejo Nacional de Investigaciones Científicas y Técnicas (CONICET)
Av. Bustillo 9500, R8402AGP, Bariloche, Argentina

[b] *Observatorio Pierre Auger, Av. San Martín Norte 304, 5613 Malargüe, Argentina*

Full author list: https://www.auger.org/archive/authors_2024_11.html

E-mail: spokespersons@auger.org

The Pierre Auger Observatory has measured the spectrum of ultra-high-energy cosmic rays with unprecedented precision, as well as the distribution of the depths of the maximum of the shower development in the atmosphere, which provide a reliable estimator of the mass composition. The measurements above $10^{17.8}$ eV can be interpreted assuming two populations of uniformly distributed sources, one with a soft spectrum dominating the flux below few EeV, and another one with a very hard spectrum dominating above that energy. When considering the presence of intense extragalactic magnetic fields between our Galaxy and the closest sources and a high-energy population with low spatial density, a magnetic horizon appears, suppressing the cosmic ray's flux at low-energies, which could explain the very hard spectrum observed at Earth. The distribution of arrival directions, which at energies above 32 EeV shows indications of a correlation with a population of starburst galaxies or the radio galaxy Centaurus A (Cen A), are also important to constrain the sources. It is shown that adding a fractional contribution from these sources of about 20% on top of an homogeneous background leads to an improvement of the model likelihood.

7th International Symposium on Ultra High Energy Cosmic Rays
(UHECR2024)
17-21 November 2024
Malargüe, Mendoza, Argentina

*Speaker

1. Introduction

The origin and acceleration mechanisms of ultra-high-energy cosmic rays (UHECRs) remain unresolved. Recent measurements by the Pierre Auger Observatory, including the energy spectrum, depth of shower maximum ($X_{\rm max}$) distributions, and arrival directions, provide key insights. Observations reveal a dipolar anisotropy above 8 EeV, pointing to an extragalactic origin, and correlations with potential source candidates such as starburst galaxies (SBG) and jetted active galactic nuclei.

This work interprets the Pierre Auger Observatory data, beginning with results from a fit across the ankle that neglects magnetic field effects. The CR flux and $X_{\rm max}$ distributions constrain CR source properties [1–3]. Observations above $10^{17.8}$ eV require two source populations: a low-energy component L, dominating below a few EeV, and a high-energy component H, dominating at higher energies. These are modeled as uniformly distributed sources with power-law spectra and rigidity-dependent cutoffs. A maximum likelihood fit suggests a high-energy spectrum harder than expected from diffusive shock acceleration (DSA), potentially explained by the suppression of low-energy CR flux due to intergalactic magnetic fields and finite inter-source distances, where the diffusion length exceeds the nearest source distance.

The final scenario combines the spectrum, $X_{\rm max}$, and arrival directions in a Bayesian framework to model UHECR emission and propagation. This approach incorporates high-energy source distributions, magnetic-field effects, and observational uncertainties, focusing on the highest energies and contributions from SBGs and Centaurus A (CenA).

2. Source models and magnetic horizon

We model the two source populations dominating at low and high energies ($y = L$ or H) using an emission rate per unit volume, time, and energy for particles of energy E, mass A, and charge Z:

$$\dot{Q}^y_A(E) = \dot{Q}^y_0 f_{A,y} \left(\frac{E}{E_0}\right)^{-\gamma_y} F_{\rm cut}\left(\frac{E}{Z\,R^y_{\rm cut}}\right), \tag{1}$$

where $\dot{Q}^y_0$ is the differential CR emission rate at a reference energy $E_0 \ll ZR^y_{\rm cut}$, and $f_{A,y}$ represents the elemental fractions (p, He, N, Si, Fe).

The rigidity cutoff function, $F_{\rm cut}$, suppresses the flux above $Z\,R^y_{\rm cut}$. We considered two shapes: a broken exponential, $F_{\rm cut}(E) = \exp(1 - E/ZR^y_{\rm cut})$ for $E > ZR^y_{\rm cut}$, or a hyperbolic secant, $F_{\rm cut}(E/Z\,R^y_{cut}) = {\rm sech}((E/Z\,R^y_{cut})^\Delta)$, where Δ controls the steepness of the cutoff.

We can define the integrated luminosity of the sources above a threshold energy E_0 (taken at $10^{17.8}$ eV) as $\mathcal{L}^y_0 = \sum_A \int_{E_0}^\infty dE\, E\dot{Q}^y_A(E)$. This allows us to introduce the integrated fractions: $I^y_A = (\int_{E_0}^\infty dE\, E\,\dot{Q}^y_A(E))/\mathcal{L}^y_0$, which allow for an easier comparison of composition between scenarios with different γ_y values.

Magnetic fields are known to permeate the Universe. Their strengths range from a few μG within galaxy clusters to less than nG in the voids between them. Therefore, any model for the propagation of UHECR should include their effect. We consider turbulent Extra Galactic Magnetic Fields (EGMFs) characterized by the root-mean-squared amplitude ($B_{\rm rms}$) and coherence length ($L_{\rm coh}$). A critical rigidity can be defined when the Larmor radius equals $L_{\rm coh}$, and is given by $R_{\rm crit} \equiv E_{\rm crit}/Z \simeq 0.9\,(B_{\rm rms}/{\rm nG})\,({\rm L_{coh}/Mpc})$ EeV, with $E_{\rm crit}$ the critical energy. It separates two propagation regimes, one at energies such that $E \ll E_{\rm crit}$ with large deflections within $L_{\rm coh}$ and a quasi-rectilinear one at higher energies. Deflections due to EGMFs result in longer travel times. For low enough source densities, or strong enough fields, particles may not have time to reach Earth from even the nearest sources, resulting in a suppression of the flux known as the magnetic horizon effect (MHE). The spectrum reaching the Earth can be obtained from that in the absence of magnetic fields by a multiplicative factor [4, 5],

$$J(E) \equiv G(E/E_{\rm crit}) J_{B=0}(E), \qquad G(x) = \exp\left[-\left(\frac{a\, X_{\rm s}}{x + b\,(x/a)^{\beta}}\right)^{\alpha}\right], \tag{2}$$

where we defined $X_{\rm s} = d_{\rm s}/\sqrt{r_{\rm H} L_{\rm coh}}$, with $r_{\rm H} = c/H_0$ the Hubble radius, and $x = E/E_{\rm crit}$. The parameters α, β, a and b depend on the evolution of the sources, whether a particle was primary or secondary, and the spectral index of the sources, as described in [5].

When including the MHE we will consider magnetic field amplitudes of $4\,{\rm nG} < {\rm B}_{\rm rms} < 100\,{\rm nG}$ and coherence lengths $25\,{\rm kpc} < L_{\rm coh} < 1\,{\rm Mpc}$, resulting in critical rigidities of $0.1\,{\rm EeV} < R_{\rm crit} < 100\,{\rm EeV}$ and $0.05 < X_{\rm s} < 4$ for source distances $3\,{\rm Mpc} < d_{\rm s} < 40\,{\rm Mpc}$. Assuming that the low-energy component originates from sources for which MHE are negligible due to a higher density, we restrict the impact of the extragalactic magnetic field (EGMF) to the high-energy component.

3. The Extended Combined Fit

We fit the measured spectrum [6] for energies above $10^{17.8}$ eV, using logarithmic bins of width $\Delta \log_{10} E = 0.1$ (with a single bin above $10^{20.5}$ eV), and the $X_{\rm max}$ distributions [7], with bins of $\Delta X_{\rm max} = 20\,{\rm g\,cm^{-2}}$ per energy interval. The source spectrum is modelled with Eq. (1), and the propagation of particles to Earth is accounted for using SimProp simulations [8], considering the photo-disintegration cross sections from TALYS [9] and the extragalactic background light model from Gilmore et al. [10]. The inferred composition from the $X_{\rm max}$ measurements relies on the hadronic interaction model, which strongly affects the conclusions [1, 3]. We test results with EPOS-LHC [11] and Sibyll 2.3d [12]. We group the nuclei at Earth by mass as: $A = 1$ (p), 2–4 (He), 5–16 (N), 17–30 (Si) and 31–56 (Fe). Nuclei arriving in their original mass group are called *primaries*, while those shifted to another group due to photo-disintegration are *secondaries*. When including MHE, we multiply the resulting flux at Earth by the suppression factor G from Eq. (2). We obtain the fit parameters maximizing a likelihood function $\mathcal{L}$, as in [1, 3]. This consists of two factors: a Gaussian term for the energy spectrum ($\mathcal{L}_J$) and a multinomial one for the $X_{\rm max}$ distributions ($\mathcal{L}_{X_{\rm max}}$), modelled using Gumbel functions dependent on the hadronic interaction model. The likelihood $\mathcal{L}$ depends on γ_y, $R^y_{\rm cut}$ and the element fractions $f_{A,y}$ for both components, together with $X_{\rm s}$ and $R_{\rm crit}$ when including the magnetic horizon effects. We report the deviance $D = -2\ln(\mathcal{L}/\mathcal{L}_{\rm sat})$, where $\mathcal{L}_{\rm sat}$ represents a model that perfectly describes the data.

Scenarios without MHE: We consider two different models for the UHECR sources. The first one assumes that the H component injects a mixture of nuclei (p, He, N, Si and Fe), while the L component injects only protons, with a galactic contribution of N nuclei at the lowest energies. The second one assumes that both source populations accelerate a mixture of nuclei. The results of the fit are summarized in Table 1. The first scenario provides a better description of the spectrum data, albeit with a hard H index and a composition dominated by mid-mass nuclei. The protons in the L

	Scenario 1		Scenario 2	
Galactic contribution (at Earth)	pure N		—	
$J_0^{\mathrm{Gal}}/(\mathrm{eV}^{-1}\,\mathrm{km}^{-2}\,\mathrm{sr}^{-1}\,\mathrm{yr}^{-1})$	$(1.06 \pm 0.04)\times 10^{-13}$		—	
$\log_{10}(R_{\mathrm{cut}}^{\mathrm{Gal}}/\mathrm{V})$	17.48 ± 0.02		—	
EG components (at the escape)	L	H	L	H
$\mathcal{L}_0/(10^{44}\,\mathrm{erg\,Mpc^{-3}\,yr^{-1}})$ *	6.54 ± 0.36	5.00 ± 0.35	11.35 ± 0.15	5.07 ± 0.06
γ	3.34 ± 0.07	-1.47 ± 0.13	3.52 ± 0.03	-1.99 ± 0.11
$\log_{10}(R_{\mathrm{cut}}/\mathrm{V})$	>19.3	18.19 ± 0.02	>19.4	18.15 ± 0.01
I_{H} (%)	100 (fixed)	0.0 ± 0.0	48.7 ± 0.3	0.0 ± 0.0
I_{He} (%)	—	24.5 ± 3.0	7.3 ± 0.4	23.6 ± 1.6
I_{N} (%)	—	68.1 ± 5.0	44.0 ± 0.4	72.1 ± 3.3
I_{Si} (%)	—	4.9 ± 3.9	0.0 ± 0.0	1.3 ± 1.3
I_{Fe} (%)	—	2.5 ± 0.2	0.0 ± 0.0	3.1 ± 1.3
D_J (N_J)	48.6 (24)		56.6 (24)	
$D_{X_{\max}}$ $(N_{X_{\max}})$	537.4 (329)		516.5 (329)	
D (N)	586.0 (353)		573.1 (353)	

* from $E_{\min} = 10^{17.8}$ eV.

Table 1: Best-fit parameters obtained in the two reference scenarios [3].

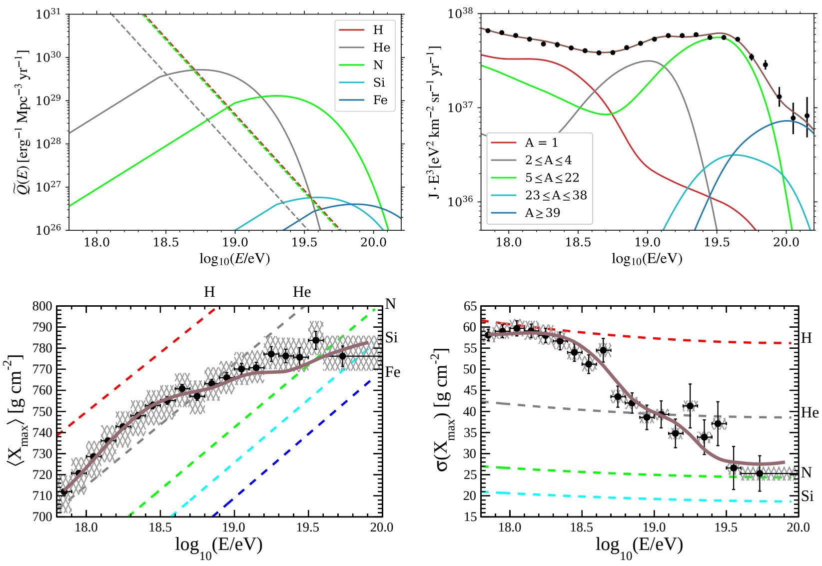

Figure 1: Scenario 2. *Top left:* Generation rate at the extragalactic sources for each representative mass; the L and H contributions are shown as dashed and solid lines, respectively. *Top right:* contributions to the energy spectrum (grouped according to mass number) at the top of the atmosphere. *Bottom:* First two moments of the $X_{\max}$ distributions as predicted by the best-fit results, along with the measured values and the predictions for pure compositions of various masses according to EPOS-LHC (dashed lines) [3].

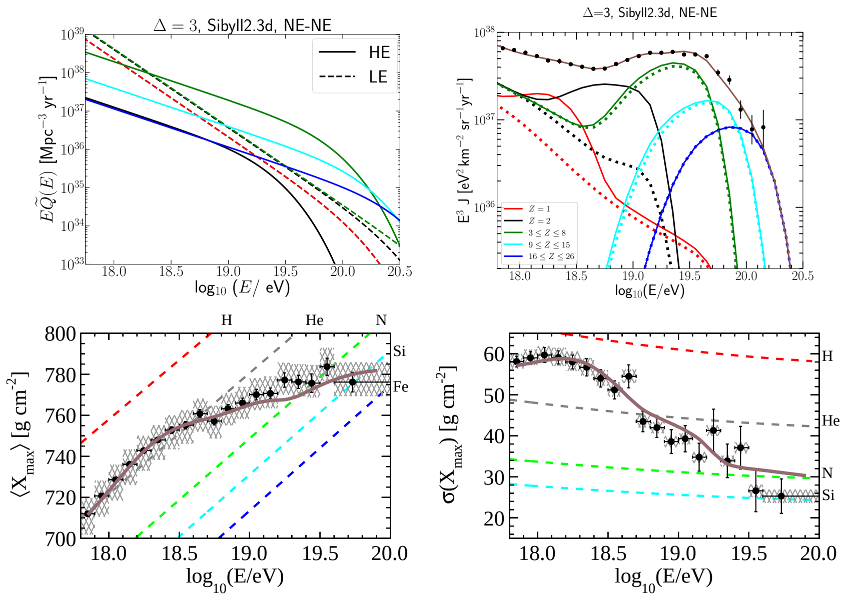

Figure 2: Analogous to 1, but for an scenario with Sibyll2.3d and a Δ = 3 cutoff including the MHE [13]

component could arise from the photo-disintegration of H nuclei. Meanwhile, the second scenario results in an overall better description of the data, due to lower deviances associated to the $X_{\max}$ measurements. Here, the L composition is dominated by protons and N nuclei, while the H one is dominated mostly by mid-mass nuclei. The H spectral index becomes even harder. Fig. 1 presents the generation rate at the sources for Scenario 2, the resulting best-fit energy spectra at Earth, and the predictions for the first two $X_{\max}$ moments, together with the data points. One can see that each H element peaks in a narrow energy range, with the composition becoming heavier for increasing energies. The ankle appears to arise from a transition between the L and H components, and the instep feature from a bump in the He contribution to the flux. The N flux dominates from the instep up to the high-energy suppression, above which we find mostly Si and Fe nuclei.

Scenarios with MHE: We present in Table 2 the results of the fits including the MHE for the different cutoff shapes and hadronic models. Sharper cutoffs lead to softer spectra and higher cutoff rigidities. For Δ = 1, the results obtained match those of scenarios without MHE [13]. Meanwhile, for sharper cutoffs, the MHE plays an important role, which results in softer H spectra, although with larger deviances. The product of the magnetic horizon parameters satisfies $X_s R_{\text{crit}} \sim 10\,\text{EeV}$.

with EGMF, NE-NE

	EPOS-LHC							Sibyll 2.3d						
Δ	γ_H	$R_{\text{cut}}^{\text{H}}$ [EeV]	γ_L	$R_{\text{cut}}^{\text{L}}$ [EeV]	X_s	R_{crit} [EeV]	D (N = 353)	γ_H	$R_{\text{cut}}^{\text{H}}$ [EeV]	γ_L	$R_{\text{cut}}^{\text{L}}$ [EeV]	X_s	R_{crit} [EeV]	D (N = 353)
1	−2.19	1.35	3.54	> 60	0	–	572	−1.67	1.42	3.37	2.21	0	–	660
2	1.03	6.02	3.62	> 51	> 3.2	1.97	583	1.35	6.22	3.53	> 25	> 3.1	1.54	635
3	1.43	7.50	3.69	> 61	2.8	2.79	614	2	7.50	3.62	> 31	2.6	3.77	640

Table 2: Parameters of the fit to the spectrum and composition including the magnetic horizon effect for the EPOS-LHC and Sibyll 2.3d hadronic interaction models and cutoff Δ = 1, 2 and 3 [13].

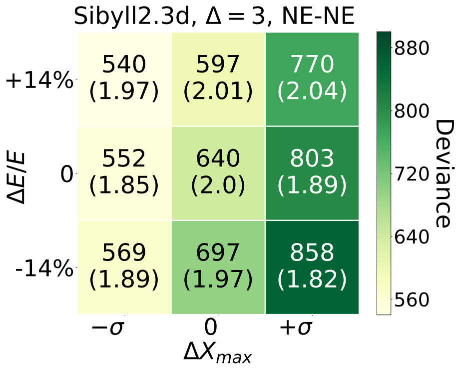

Figure 3: Deviance (and H spectral index) obtained from the fit when shifting $\pm\sigma_{\rm sys}$ in the energy and $X_{\rm max}$ scales for the Sibyll2.3d and $\Delta = 3$ cutoff scenario [13].

Changing from EPOS-LHC to the Sibyll2.3d model produces softer spectra and larger deviances. However, for the Sibyll2.3d model, scenarios with an significant MHE result in lower deviances than their no MHE counterpart [13]. The best fit results for $\Delta = 3$, which leads to $\gamma_H = 2$, are shown in Fig. 2. The top left panel presents the generation rate per mass group, showing the soft injection spectra of the H component. The top right panel presents the resulting spectra at Earth, which is quite similar to the one found in Fig. 1, but features a substantial contribution of He from the L component and Si for the H one. The results for the composition measurements are displayed on the bottom panels with the model predictions closely matching the observations.

Systematics effects on the energy and $X_{\rm max}$ scale calibration affect the results of the fits. Fig. 3 presents the deviance and the H spectral index obtained when shifting the energy and $X_{\rm max}$ scales by $\pm\sigma_{\rm sys}$. A positive shift in energy and/or a negative one in $X_{\rm max}$ reduce the deviance, sometimes by almost 100 units. In general, positive shifts in the $X_{\rm max}$ scale are strongly disfavoured. In all cases, the H spectral index remains close to 2.

4. Combined Fit including arrival directions

Since arrival directions show correlations with catalogs of extragalactic source candidates [14], an extension of the analysis was performed in [15] including a fraction of the H flux from catalog sources. The analysis focused on the highest energies, performing the fit to the spectrum and $X_{\rm max}$ above 10^{19} eV and the arrival directions above $10^{19.2}$ eV, and only one (H) component was considered, with injection parameters shared between catalog and background sources. Different source cosmological evolutions are considered, multiplying Eq. 1 by $(1+z)^m$, where z is the redshift and m the cosmological evolution index. Two new fit parameters are included, f_0, which represents the fraction of the flux from catalogue sources at 40 EeV, and δ_0, which stands for the blurring of protons at 10 EeV due to EGMFs. The likelihood has now three independent terms: $\mathcal{L}_{\rm AD}$ which compares the flux map coming from the assumed sources with the actual data in the different energy bins, $\mathcal{L}_{\rm J}$, a Poissonian likelihood for the spectrum, and a multinomial one for the $X_{\rm max}$ distributions, modelled using Gumbel functions dependent on the hadronic interaction model.

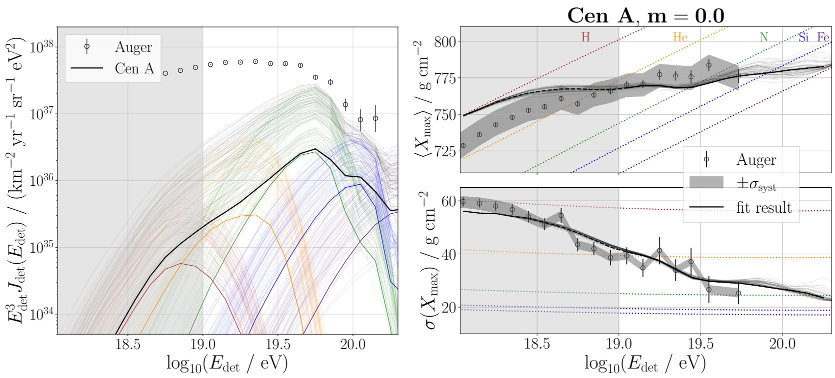

Figure 4: *Left:* Cen A contribution to the flux. *Right:* First two moments of the $X_{\max}$ distributions [15].

Table 3 presents the results for two catalogs, one of starburst galaxies (SBG) and another containing just the radio-galaxy Cen A. We present the best-fit result as well as the posterior mean and the highest posterior density interval. In all cases, we found very hard H spectra with very low cutoff rigidities. The spectrum becomes even harder for strong source cosmological evolutions, reaching $\gamma = -3$ in some cases, as reported in [15]. The contribution of cataloged sources f_0 varies from $\sim$ 3% or 19% and the magnetic blurring parameter δ_0 is larger than $\sim 15°$ in all scenarios. The Cen A scenario with a flat cosmological evolution provides the best fit. The left panel of Fig. 4 presents the spectrum at Earth separated by mass group (each thin line sampled from the posterior distribution), a black line representing the Cen A contribution. The right panel shows the first two $X_{\max}$ moments as proxies for the composition fit results.

	Cen A, m = 0 (flat)		**Cen A, m = 3.4** (SFR)		**SBG, m = 3.4** (SFR)	
	posterior	MLE	posterior	MLE	posterior	MLE
γ	$-1.67^{+0.48}_{-0.47}$	-2.21	$-3.09^{+0.23}_{-0.24}$	-3.05	$-2.77^{+0.27}_{-0.29}$	-2.67
$\log_{10}(R_{\rm cut}/{\rm V})$	$18.23^{+0.04}_{-0.06}$	18.19	$18.10^{+0.02}_{-0.02}$	18.11	$18.13^{+0.02}_{-0.02}$	18.13
f_0	$0.16^{+0.06}_{-0.14}$	0.028	$0.05^{+0.01}_{-0.03}$	0.028	$0.17^{+0.06}_{-0.08}$	0.19
$\delta_0/°$	$56.5^{+29.4}_{-12.8}$	16.5	$27.6^{+2.7}_{-16.3}$	16.8	$22.2^{+5.3}_{-4.0}$	24.3
$I_{\rm H}$	$5.9^{+2.5}_{-1.7}\times10^{-2}$	7.1×10^{-2}	$8.3^{+2.0}_{-8.3}\times10^{-3}$	1.6×10^{-5}	$6.4^{+1.3}_{-6.4}\times10^{-3}$	4.3×10^{-5}
$I_{\rm He}$	$2.3^{+0.3}_{-0.5}\times10^{-1}$	1.9×10^{-1}	$1.3^{+0.2}_{-0.2}\times10^{-1}$	1.4×10^{-1}	$1.7^{+0.3}_{-0.4}\times10^{-1}$	1.8×10^{-1}
$I_{\rm N}$	$6.3^{+0.3}_{-0.3}\times10^{-1}$	6.2×10^{-1}	$7.4^{+0.3}_{-0.3}\times10^{-1}$	7.3×10^{-1}	$7.4^{+0.3}_{-0.3}\times10^{-1}$	7.4×10^{-1}
$I_{\rm Si}$	$6.5^{+3.6}_{-3.3}\times10^{-2}$	9.9×10^{-2}	$9.2^{+3.2}_{-2.3}\times10^{-2}$	1.1×10^{-1}	$5.7^{+2.5}_{-3.1}\times10^{-2}$	5.4×10^{-2}
$I_{\rm Fe}$	$1.6^{+0.7}_{-1.0}\times10^{-2}$	2.0×10^{-2}	$2.5^{+0.8}_{-0.9}\times10^{-2}$	2.3×10^{-2}	$2.5^{+0.8}_{-0.9}\times10^{-2}$	2.3×10^{-2}
$\boldsymbol{D_E}$ (N_J = 14)		22.3		28.5		33.3
$\boldsymbol{D_{X_{\max}}}$ ($N_{X_{\max}}$ = 74)		124.9		130.6		126.2
$\boldsymbol{D}$		147.2		159.1		159.5
log $\boldsymbol{\mathcal{L}_{\rm ADs}}$		10.5		10.4		13.3
log $\boldsymbol{\mathcal{L}}$		-239.1		-245.1		-242.4

Table 3: Fit results for the Centaurus A and SBG models. The best-fit (MLE) parameters and the corresponding deviance D and log-likelihood values $\log\mathcal{L}$ are stated. Also, the posterior mean and highest posterior density interval from the MCMC sampler are given [15].

5. Conclusions

We presented a summary of recent developments on the interpretation of the spectrum, composition, and arrival direction data as measured by the Pierre Auger Observatory. Using two distinct source populations modelled with power-law emissions, we performed a Combined Fit to the spectrum and composition data. This method successfully reproduced the observed measurements.

However, the resulting H energy spectral index is very hard, which is inconsistent with the expectations from DSA. We showed that including the propagation effect of EGMFs and a finite distance to the nearest sources can alleviate this tension. The fit can be refined even further by shifting the energy scale by +14% and the X_{max} measurements by $-\sigma_{\mathrm{sys}}$.

Furthermore, since $X_{\mathrm{s}}R_{\mathrm{crit}} \sim 5 - 10\,\mathrm{EeV}$ whenever the MHE plays an important role, in these type of scenarios the source density and magnetic field parameters should satisfy

$$X_{\mathrm{s}}R_{\mathrm{crit}} \simeq 5\,\mathrm{EeV}\frac{d_{\mathrm{s}}}{20\,\mathrm{Mpc}}\frac{B_{\mathrm{rms}}}{100\,\mathrm{nG}}\sqrt{\frac{L_{\mathrm{coh}}}{25\,\mathrm{kpc}}}. \quad (3)$$

We then explored an astrophysical model that included also the information from the arrival directions above 16 EeV. Scenarios with a fraction of UHECRs coming from the radiogalaxy Cen A or a starburst galaxies catalog provided a better fit than a homogeneous flux model. All models had a very hard H spectrum. The best fit fraction of the flux from the catalog varied between $\sim 3\%$ and 19%, with large uncertainties, and a blurring larger than 15° was preferred.

References

[1] A. Aab *et al.* [Pierre Auger Collaboration], JCAP **04** (2017) 038.

[2] A. Aab *et al.* [Pierre Auger Collaboration], PoS(ICRC2021)311.

[3] A. Aab *et al.* [Pierre Auger Collaboration], JCAP**05** (2023) 024.

[4] S. Mollerach and E. Roulet, JCAP **10** (2013) 013.

[5] J. González, S. Mollerach and E. Roulet, Phys. Rev. D **104** (2021) 063005.

[6] A. Aab *et al.* [Pierre Auger Collaboration], Eur. Phys. J. C **81** (2021) 966.

[7] A. Yushkov (for the Pierre Auger Collaboration) PoS(ICRC2019)482.

[8] R. Aloisio *et al.*, JCAP **11** (2017) 009.

[9] A.J. Koning, S. Hilaire and M.C. Duijvestijn, AIP Conference Series **769** (2005) 1154.

[10] R. Gilmore, R. Somerville, J. Primack and A. Domínguez, MNRAS **442** (2012) 3189.

[11] T. Pierog *et al.* , Phys. Rev. C **92** (2015) 034906.

[12] F. Riehn, R. Engel, A. Fedynitch, T. K. Gaisser and T. Stanev, Phys. Rev. D **102** (2020) 063002.

[13] A. Aab *et al.* [Pierre Auger Collaboration], JCAP**07** (2024) 094.

[14] A. Aab *et al.* [Pierre Auger Collaboration], ApJ **935** (2022) 179

[15] A. Aab *et al.* [Pierre Auger Collaboration], JCAP**01** (2024) 022.

PoS(UHECR2024)015